

| | |
|--------------|---|
| Title | Modified cellular automaton simulation of metal additive manufacturing |
| Author(s) | Kubo, Jun; Koizumi, Yuichiro; Ishimoto, Takuya et al. |
| Citation | Materials Transactions. 2021, 62(6), p. 864-870 |
| Version Type | VoR |
| URL | https://hdl.handle.net/11094/89892 |
| rights | |
| Note | |

Osaka University Knowledge Archive : OUKA

<https://ir.library.osaka-u.ac.jp/>

Osaka University

Modified Cellular Automaton Simulation of Metal Additive Manufacturing*¹

Jun Kubo^{1,*2}, Yuichiro Koizumi², Takuya Ishimoto² and Takayoshi Nakano^{2,*2}

¹CAPCAST Inc., Shimotsuke 329-0434, Japan

²Division of Materials and Manufacturing Science, Graduate School of Engineering, Osaka University, Suita 565-0871, Japan

Metal additive manufacturing (AM) technologies are attracting attentions not only as a fabrication process of complicated three-dimensional parts but also as microstructure controlling processes. In powder bed fusion (PBF)-type AM, crystallographic texture can be controlled by scanning strategies of energy beam. To optimize microstructures, computer simulations for predicting microstructures play very important roles. In this work, we have developed simulation programs to explain the mechanism of the crystal orientation control. First, we simulated the shape of melt pool by analyzing the heat transfer using apparent heat conductivity when the penetration of laser beam through keyholes was taken into consideration because of the evaporation and accompanying convections. It was assumed that the primary crystal growth direction can be determined by the temperature gradient, and the crystals grow keeping the growth direction as generally recognized. The shapes of simulated melt pools agree well with experimental observations. The modified cellular automaton simulations successfully reproduced two typical textures with different preferential orientations along the building directions of $\langle 100 \rangle$ and $\langle 110 \rangle$ when the bidirectional scanning with and without a rotation of 90° , respectively, was accomplished between the layers. [doi:10.2320/matertrans.MT-M2021009]

(Received January 19, 2021; Accepted March 12, 2021; Published April 16, 2021)

Keywords: additive manufacturing, simulation, melt pool, crystallographic texture

1. Introduction

Recently, the application of metal-additive manufacturing (AM) has been extended to various fields. Metal AM, which is characterized by a bottom-up additive production of parts, has been developed as a means of producing three-dimensional structures with complex shapes. Furthermore, this technique has been proven to be extremely useful for controlling the microstructure of metallic materials, particularly their crystallographic textures.^{1–5} Crystallographic texture is a significant metallographic feature that governs mechanical properties such as Young's modulus¹ and yield stress,⁴ and chemical properties such as oxidation resistance,⁵ of metals independently of shape. Its flexible control is indispensable for enhancing the functionality of metallic parts.

Computer simulations are becoming increasingly necessary in a wide variety of areas such as shape optimization of fabricated objects (topology optimization),⁶ optimization of support shapes and fabrication patterns,⁷ prediction of residual stress,⁸ elucidation of the causes of pores,⁹ and functional evaluation based on the geometry of a fabricated object.¹⁰ However, the crystallographic texture evolution mechanism, which is directly linked to the functionality of metallic materials, and computer simulations to control this mechanism have not been established yet because metal AM is a technique based on rapid melting and solidification in units of minute melt pools formed by the scanning of the energy beams. Simulations are generally performed assuming various physical phenomena and physical quantities because *in situ* observation and measurement during process are extremely difficult.

This study focuses on the crystallographic orientation formation behavior, which depends on the laser scan strategy

(combination of laser scanning directions for each layer) using the selective laser melting (SLM) method for β -type titanium alloys with a bcc structure, and aims at elucidating the formation mechanism by implementing simulations based on the cellular automaton (CA) method. Presently, most of the simulations performed to study the crystallographic texture in metal AM focus on predicting the crystal growth direction and formation of grains such as columnar and equiaxed grains.¹¹ In contrast, this study thoroughly investigated the evolution process of the crystallographic orientation by improving the conventional CA method.

2. Texture Evolution of β -Type Titanium Alloy (Ti–15Mo–5Zr–3Al) Depending on the Laser Scan Strategy under SLM

Figure 1 depicts the crystallographic texture evolution behavior of the Ti–15Mo–5Zr–3Al alloy (mass%) in SLM fabrication. The observed crystallographic orientations differed significantly simply by changing the scanning strategy of the laser beam. In the case where the laser scans only along the X-axis (scan strategy X), texture formation with predominate orientation of $\langle 100 \rangle$ in the X (scan) direction and $\langle 110 \rangle$ in Y and Z directions were observed. In contrast, in case where the laser scan direction was alternately changed to X- and Y-axes (scan strategy XY), $\langle 100 \rangle$ aligned in all X, Y, and Z directions. The factors affecting the formation of crystallographic orientation caused by these laser scanning patterns were investigated using simulation.

3. Analysis Methods

The SLM process using the Ti–15Mo–5Zr–3Al alloy was analyzed in this study. Computations were performed primarily for analyzing heat transfer and crystallographic orientation during the fabrication.

3.1 Heat transfer analysis

In the heat transfer analysis, the change in temperature

*¹This Paper was Originally Published in Japanese in J. Japan Inst. Met. Mater. **85** (2021) 103–109.

*²Corresponding authors, E-mail: j-kubo@capcast.co.jp, nakano@mat.eng.osaka-u.ac.jp

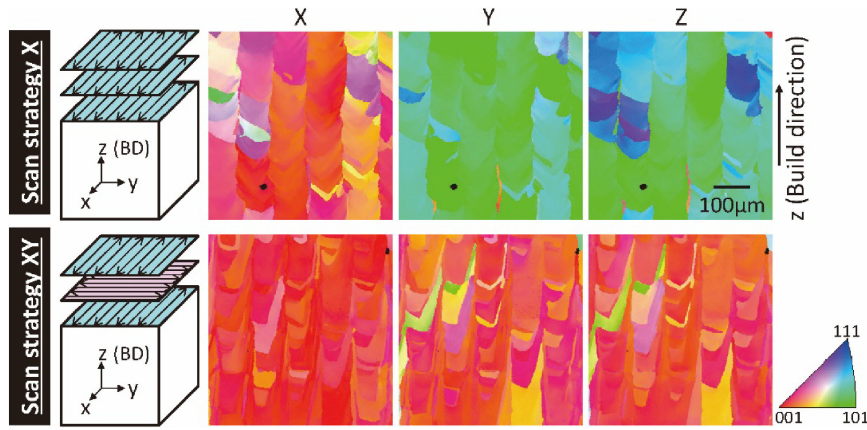


Fig. 1 Experimental inverse pole figure (IPF) maps¹⁾ on the vertical cross sections (y-z plane) of beta-type Ti-15Mo-5Zr-3Al alloy fabricated by SLM with scan strategy X (without rotation) and scan strategy XY (with 90° rotation). [after T. Ishimoto *et al.*¹⁾].

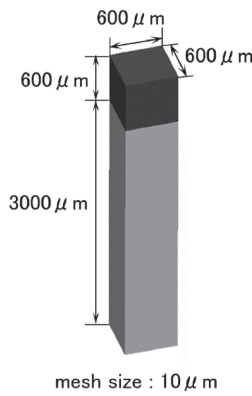


Fig. 2 FEM model for analysis.

distribution over time was calculated by solving the heat conduction equation given below.¹²⁾ The modification factors were adjusted so that the melt pool shape agreed with that of the experimental results because probable effects such as those due to convection and evaporation cannot be expressed in eq. (1).

$$c\rho \frac{\partial T}{\partial t} = \lambda \left(l \frac{\partial^2 T}{\partial x^2} + m \frac{\partial^2 T}{\partial y^2} + n \frac{\partial^2 T}{\partial z^2} \right) - \rho L \frac{\partial f_L}{\partial t}, \quad (1)$$

where c is the specific heat; ρ is the density; T is the temperature; t is the time; λ is the thermal conductivity; L is the latent heat; f_L is the liquid phase fraction; and l , m , and n are the modification factors considering the anisotropy of heat transfer.

The analysis was performed based on a finite element method (FEM). As depicted in Fig. 2, a cuboid with a base part 3 cm in height placed below the fabrication part of 600 µm × 600 µm × 600 µm dimensions was modeled with a 10 µm size mesh. Table 1 lists the parameters used in the simulation. A value smaller than the heat transfer coefficient between metals commonly used in casting analysis and greater than the heat transfer coefficient between metal and air (4188.0 W·m⁻²·K⁻¹) was used in the analysis¹³⁾ because the heat transfer coefficient, which is the boundary condition between the fabrication part and the surrounding metal powder, is unknown. Moreover, the validity of the analysis results was confirmed by comparing the melt pool shapes obtained via actual experiments because the actual measure-

Table 1 Parameters used for simulation.

| | |
|---------------------------------|-----------------------------|
| Density | 5010.0 [kg/m ³] |
| Specific heat | 540.1 [J/kg.K] |
| Conductivity | 7.496 [W/m.K] |
| Latent heat | 389.4 [kJ/kg] |
| Liquidus temperature | 1933.0 [K] |
| Solidus temperature | 1843.0 [K] |
| Modification factor (l) | 1.0 |
| Modification factor (m) | 1.0 |
| Modification factor (n) | 200.0 |
| Input energy | 360.0 [W] |
| Scanning speed | 1200.0 [mm/s] |
| Scan pitch | 0.1 [mm] |
| Thickness | 0.06 [mm] |
| Time for supplying powder layer | 1.0 [s] |

ment of temperature distribution changes is difficult in the SLM process with an ultrahigh cooling rate.^{14,15)}

3.2 Crystallographic orientation analysis

As depicted in Fig. 1, crystallographic orientations differ based on the scan strategy of the laser beam. The underlying reason was investigated by referring to the classic solidification theory. Considering the columnar and equiaxed grains observed in general solidification, as depicted in the schematic in Fig. 3,^{16,17)} the crystal growth in the initial period of solidification proceeds in the direction of the thermal gradient perpendicular to the isothermal plane. It is generally known that, even when solidification begins with crystals having fine random orientations like chill crystals, the crystals with the preferential growth orientation (orientation of $\langle 100 \rangle$ for the cubic crystal) aligned with the thermal gradient direction grows preferentially. However, even when the preferential growth direction is oriented in the direction of the thermal gradient, various columnar crystals do grow having orientations that differ because of the rotation around the growth direction. Moreover, when the direction of the thermal gradient changes with the progress of solidification and the directions of the preferential growth

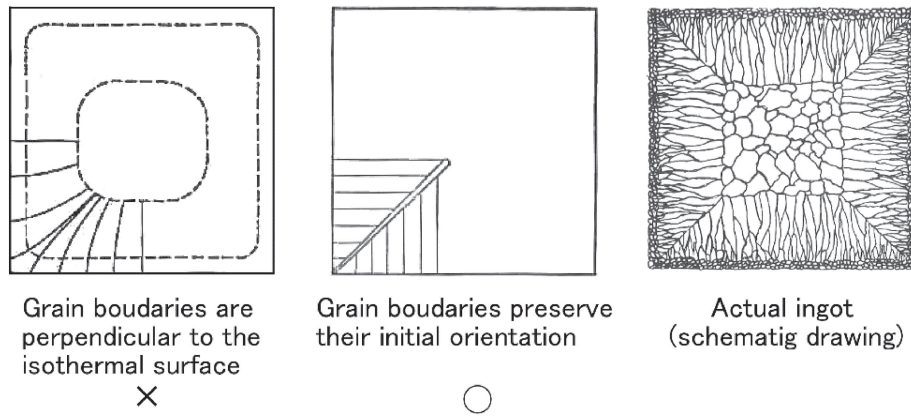


Fig. 3 Schematic illustrations of crystal growth in casting [after Chalmers¹⁵⁾ and Flemings¹⁶⁾].

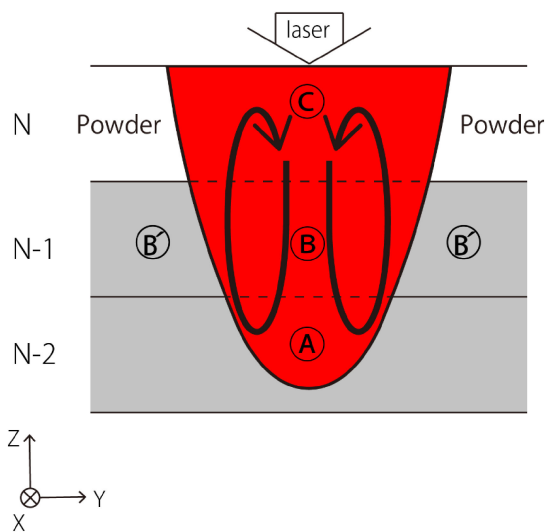


Fig. 4 Schematic illustrations of Nth layer melt pool.

thermal gradient of the crystals are different, growth does not occur along the preferential growth direction oriented in the thermal gradient direction as in the initial solidification. Under such conditions, it is widely known that the growth of crystals continues even under unfavorable thermal gradients when the supercooling rate is low and new crystal nuclei are not generated. These were considered in interpreting the experimental results depicted in Fig. 1.

It is likely that a state as depicted in the schematic in Fig. 4 will occur when the deepest point of the melt pool caused by the laser beam for layer N reaches layer N-2. New crystal nuclei are generated in the interface between the C region and the powder because columnar grains do not grow from the unmelted powder. The initial growth for such crystals orients in the thermal gradient direction as depicted in Fig. 3. At this time, if there is no effect of convection, the thermal gradient direction will be perpendicular to the interface between the C region and the powder. Because convection actually occurs as depicted in Fig. 4, it is likely that the inclination increases further. In this study, this convection effect was modeled by increasing the apparent thermal conductivity in the Z direction by introducing the modification factors listed in Table 1 in eq. (1). Moreover, the solid-liquid interface is nearly parallel to the scan direction because the laser scan

speed in metal AM is mostly greater than the migration rate of the solid-liquid interface. Accordingly, for both the X and XY scan strategies, in region C in Fig. 4, the $\langle 100 \rangle$ direction aligns with the laser scan direction (X direction in Fig. 4); the $\langle 110 \rangle$ direction aligns for other directions (Y and Z directions in Fig. 4).

Figure 5(a) depicts the schematic of layer N + 1 for scan strategy X. In this illustration, region C' is identical as region C in Fig. 4, and the crystallographic texture where $\langle 100 \rangle$ orients in the X direction and $\langle 110 \rangle$ orients in Y and Z directions is formed. Regarding the solidification in the C region, when no new nuclei are generated at the interface between C and C' regions as explained earlier, the preferential growth direction of the adjacent C' region is inherited. Similar to the C' region, columnar grains grow and $\langle 100 \rangle$ orients in the X direction and $\langle 110 \rangle$ orients in Y and Z directions (Fig. 5(a) lower row). Because the layers are added in this manner, for all the layers in scan strategy X, the primary orientation is always $\langle 100 \rangle // X$ direction and $\langle 110 \rangle // Y$ and Z directions.

Figure 5(b) depicts the schematic of layer N + 1 for scan strategy XY. Similar to the scan strategy X, region C' in Fig. 5(b) represents region C ($\langle 100 \rangle // X$ direction and $\langle 110 \rangle // Y$ and Z directions) in Fig. 4. A magnified schematic of the interface between C and C' regions is illustrated in the lower row in Fig. 5(b). The crystallographic orientation in the C' region adjacent to the melt surface differs from that depicted in Fig. 5(a) because, compared with Fig. 5(a), there is a rotation of 90° around the Z-axis in Fig. 5(b). As described previously, when no nuclei are generated in the interface between C and C' regions, columnar grains grow by inheriting the preferential direction of growth of the adjacent unmelted region (C' region). In such a case, although one of the $\langle 100 \rangle$ (e.g. $[100]$) is fixed in the X directions in Fig. 5(b), the other two $\langle 100 \rangle$ (e.g. $[010]$ and $[001]$) remain to be undetermined. As described previously, for the growth of columnar grains, the preferential growth direction is more dominant than the thermal gradient direction. Accordingly, for the other two $\langle 100 \rangle$ directions that are not primal, the following was considered assuming that they are affected by the thermal gradient. For scan strategy X where the thermal gradient direction is nearly parallel to the preferential growth direction, it was assumed that no rotation about the preferential growth direction occurred without being affected

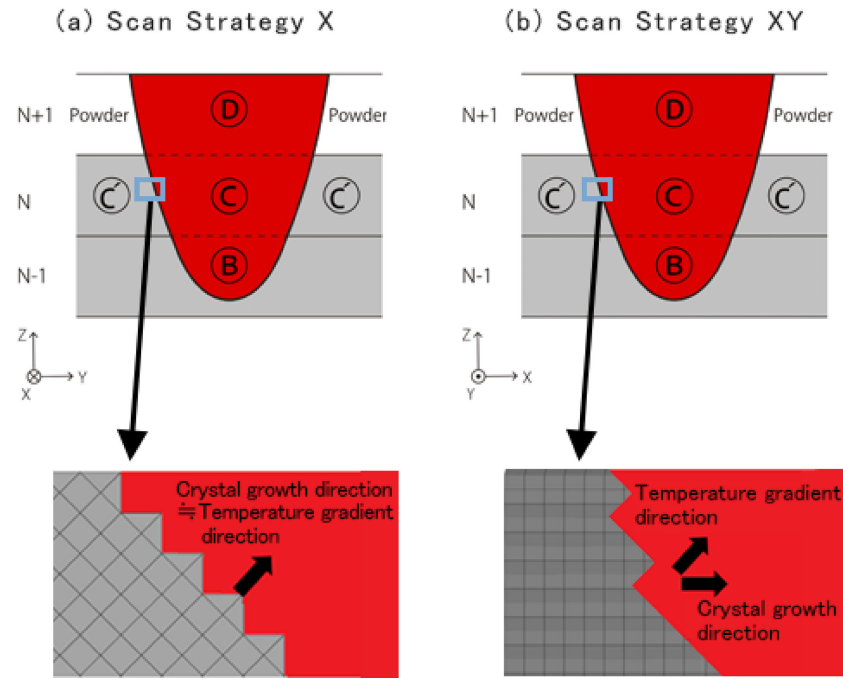


Fig. 5 Schematic illustrations of (N + 1)th layer melt pool. (a) scan strategy X, (b) scan strategy XY.

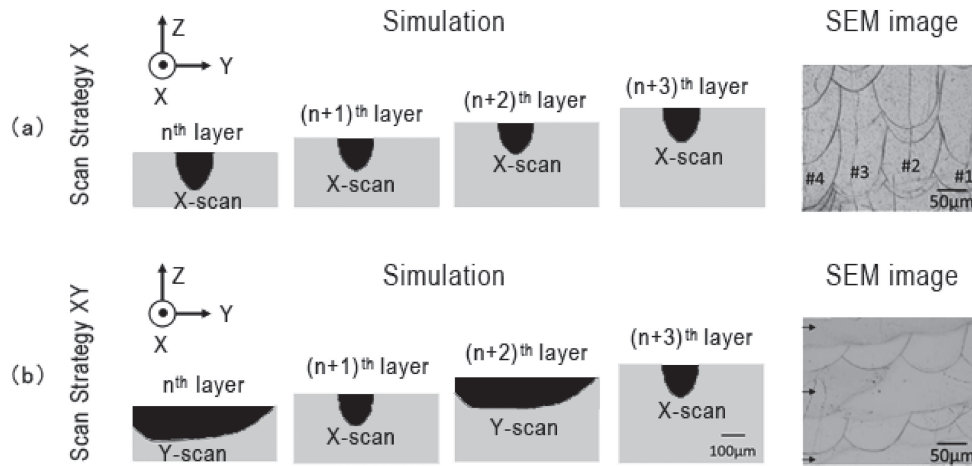


Fig. 6 Comparison between the geometries of simulated melt pools and fusion lines experimentally observed by SEM (after Ishimoto *et al.*¹⁾).

by the thermal gradient direction. In contrast, for the scan strategy XY, where the thermal gradient direction and the preferential growth direction are significantly different, it was assumed that rotation around the preferential growth direction occurred. In particular, the plane containing the preferential growth direction vector and the thermal gradient direction vector was estimated, and the second $\langle 100 \rangle$ direction was set as the direction within the same plane perpendicular to the preferential growth direction. Determining the two $\langle 100 \rangle$ directions enables determining the third direction of $\langle 100 \rangle$.

In the simulation, first, the temperature at each time interval was calculated using heat transfer analysis. When the temperature dropped below the solidus temperature, if there were no elements nearby with the temperature lower than the solidus temperature, crystal nuclei were generated, and its growth direction corresponded to the thermal gradient direction. In contrast, when the temperature dropped below

the solidus temperature for an element and there was another nearby element with a temperature lower than the solidus temperature, the growth direction of that element was inherited. In this manner, the crystal structure was generated over time by adopting the idea similar to the CA method,^{18,19)} where the change of state of an element is determined sequentially from the state of an adjacent element. The other $\langle 100 \rangle$ directions different from the crystal growth direction were also calculated using the thermal gradient along the plane perpendicular to the laser beam scanning direction.

4. Results of the Simulation

4.1 Heat transfer analysis

Figure 6 depicts a comparison between the shapes of the simulated melt pools and experimentally observed fusion lines on the cross sections of the products. For scan strategies

X and XY, the simulated shapes of the melt pools agree well with the actual fusion lines observed in the products. In the simulation, U-shaped melt pools is confirmed in the cross-section perpendicular to the laser scan direction. This corresponds to the scale-like pattern (fusion lines) observed across the whole cross section in the product fabricated with scan strategy X. Also in scan strategy XY, fusion lines formed by laser scan along both X direction (scale-like shape) and Y direction (elongated shape in Y direction) are well reproduced.

4.2 Crystallographic orientation distribution

Figures 7 and 8 depict the simulation results for scan strategy X. Figure 7 depicts the results of the first few layers of fabrication. Only the unmelted region is shown. Figure 8 depicts the comparison of the simulated orientation map (lower row) with the inverse pole figure (IPF) map obtained from the actual product (upper row). The simulation results are illustrated in color by calculating $\cos \phi$, where ϕ is the angle between the $\langle 100 \rangle$ direction. Accordingly, the red ($\phi = 0^\circ$) and green ($\phi = 45^\circ$) indicate $\langle 100 \rangle$ and $\langle 110 \rangle$, respectively, as represented in the color bar. The simulation

results mostly reproduce the actual crystallographic texture where the $\langle 100 \rangle$ preferentially orients in the X direction and $\langle 110 \rangle$ orients in the Y and Z directions. As depicted in Fig. 8 (upper row), near $\langle 111 \rangle$ orientation depicted in blue or purple partly appears in the X and Z directions. The likely reason of this is that the solid-liquid interface was not completely parallel to the direction of laser scanning; however, the underlying factors need to be studied further. In the simulation, because the laser scan speed was fast enough to result in the solid-liquid interface being nearly parallel to the scanning direction, no orientation in the $\langle 111 \rangle$ direction was observed. Moreover, grains with $\langle 100 \rangle$ orientation in the Y and Z directions have grown (the red vertical lines in Fig. 8 lower row). These grains extend directly from the melt pool bottom and grow in the build direction (Z direction). As a result, grain boundaries parallel to the Z direction generate. It is likely that, because the melt pool depicted in Fig. 6 has a large curvature radius at the bottom, crystals have grown upward from the melt pool center (bottom). When the curvature radius at the melt pool bottom is small, even if grains oriented in the Z direction grow there, they are eliminated by the grains grew from the melt pool sides with $\langle 110 \rangle // Z$ orientation.^{4,20} Such grains are also observed in the actual product as shown in the upper row of Fig. 8. In this manner, grains grow from both sides of the melt pool generating grain boundaries in the central region of the melt pool.

Figures 9 and 10 depict the simulation results for scan strategy XY. Figure 9 depicts the results of the first few layers of fabrication. Only the solid phase was colored to indicate the crystal orientation, the liquid phase was hidden, and the solid-liquid interface was shown in brown. Since it is a three-dimensional map, the solid-liquid interface behind the hidden liquid phase is visible in brown.

For scan strategy XY, Fig. 10 depicts the comparison of the simulated final orientation map with the IPF map obtained from the actual product. As depicted in Fig. 9, similar to scan strategy X, initially, grains with $\langle 110 \rangle // Z$ direction (green) appear, which remelt thereafter to produce new grains with $\langle 100 \rangle // Z$ direction. As a result, the most regions represent the crystallographic orientation where $\langle 100 \rangle$ preferentially orients in X, Y, and Z directions. The orientation with $\langle 110 \rangle // Z$ is also observed at the topmost part; it is probably owing to the nonoccurrence of remelting and resolidification. Moreover,

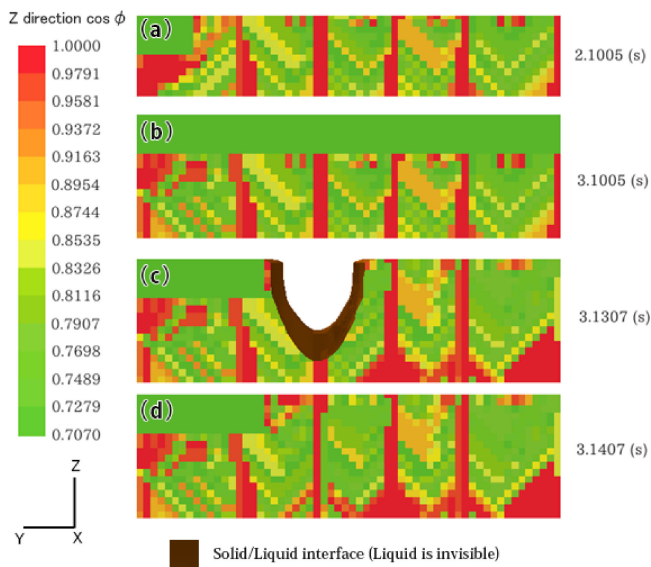


Fig. 7 Early analysis results of scan strategy X at (a) 2.1005 s, (b) 3.1005 s, (c) 3.1307 s, (d) 3.1407 s.

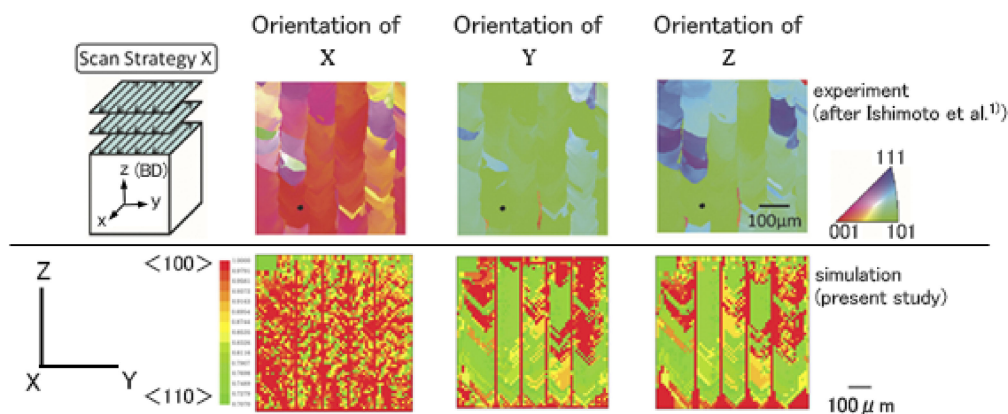


Fig. 8 Comparison of analysis results (lower side) with experimental results (upper side: after Ishimoto *et al.*¹⁾) of scan strategy X.

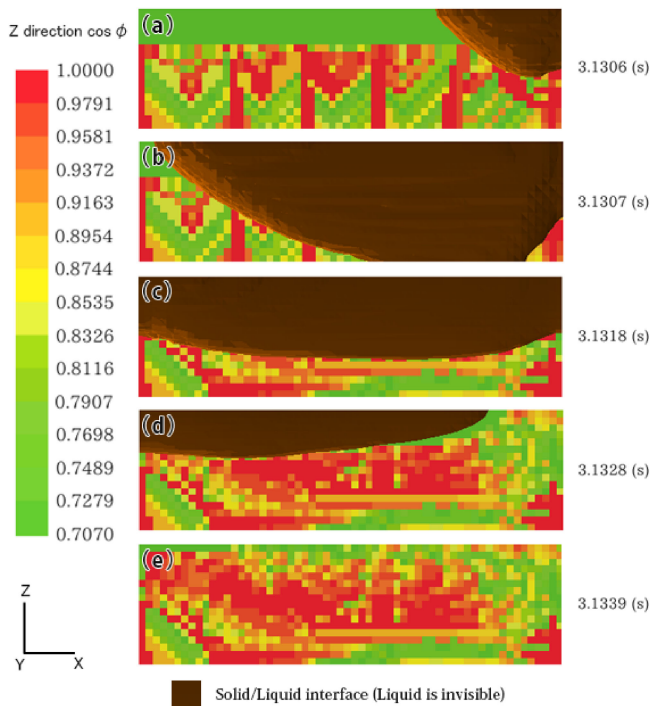


Fig. 9 Early analysis results of scan strategy XY at (a) 3.1306 s, (b) 3.1307 s, (c) 3.1318 s, (d) 3.1328 s, (e) 3.1339 s.

for the Y and Z directions, $\langle 110 \rangle$ orientation is seen, though less frequently. This would be because the values used in the simulation were different from the actual ones. The physical properties of the powder material and the interface conditions (heat transfer coefficients) for the melt pool are poorly understood. To improve accuracy of simulation of metal AM, measurement of the real phenomenon is needed, although it is challenging.

5. Conclusion

In this study, the SLM fabrication of metals with cubic crystal structures was investigated to elucidate the underlying mechanism of crystallographic texture evolution, where distinct crystallographic orientations occur depending on scan strategies. The process of crystal growth in the melt pool created by laser scanning was modeled based on the published experimental observations, classic solidification

theory, and casting solidification simulation technique. The model was then solved using the cellular automaton method to analytically reproduce the characteristic crystallographic orientation distributions. Since it is extremely difficult to observe the real phenomenon because metal AM involves ultrahigh speed and superfine regions, the simulation was effective to understand how the crystallographic orientation evolves. However, further studies are required to improve the accuracy of the calculations by improving the accuracy of parameters such as interface conditions and material properties. In addition, further studies are required to compare the experimental results with analytical (simulation) results for a wide variety of alloy compositions and fabrication conditions.

Acknowledgments

This work was supported by Grants-in-Aid for Scientific Research from the Japan Society for the Promotion of Science (JSPS) [grant number JP18H05254].

REFERENCES

- 1) T. Ishimoto, K. Hagihara, K. Hisamoto, S.-H. Sun and T. Nakano: *Scr. Mater.* **132** (2017) 34–38.
- 2) S.-H. Sun, K. Hagihara and T. Nakano: *Mater. Des.* **140** (2018) 307–316.
- 3) K. Hagihara, T. Nakano, M. Suzuki, T. Ishimoto, Suyalatu and S.-H. Sun: *J. Alloy. Compd.* **696** (2017) 67–72.
- 4) S.-H. Sun, T. Ishimoto, K. Hagihara, Y. Tsutsumi, T. Hanawa and T. Nakano: *Scr. Mater.* **159** (2019) 89–93.
- 5) O. Gokcekaya, N. Hayashi, T. Ishimoto, K. Ueda, T. Narushima and T. Nakano: *Addit. Manufact.* **36** (2020) 101624.
- 6) Y. Saadlaoui, J.-L. Milan, J.-M. Rossi and P. Chabrand: *J. Manuf. Syst.* **43** (2017) 178–186.
- 7) M. Langelaar: *Struct. Multidiscipl. Optim.* **57** (2018) 1985–2004.
- 8) L. Parry, I.A. Ashcroft and R.D. Wildman: *Addit. Manufact.* **12** (2016) 1–15.
- 9) B. Cheng, L. Loeber, H. Willeck, U. Hartel and C. Tuffile: *J. Mater. Eng. Perform.* **28** (2019) 6565–6578.
- 10) T. Maconachie, M. Leary, B. Lozanovsky, X. Zhang, M. Qian and O. Faruque: *Mater. Des.* **183** (2019) 108137.
- 11) R. Shi, S. Khairallah, T.W. Heo, M. Rolchigo, J.T. Mckeown and M.J. Matthews: *JOM* **71** (2019) 3640–3655.
- 12) K. Kubo and R.D. Pehlke: *Metall. Trans. B* **16** (1985) 359–366.
- 13) I. Ohnaka: *Computer Dennetsu Gyouko Kaiseki Nyumon*, (Maruzen, Tokyo, 1985) p. 339.
- 14) A. Klassen, T. Scharowsky and C. Kömer: *J. Phys. D* **47** (2014)

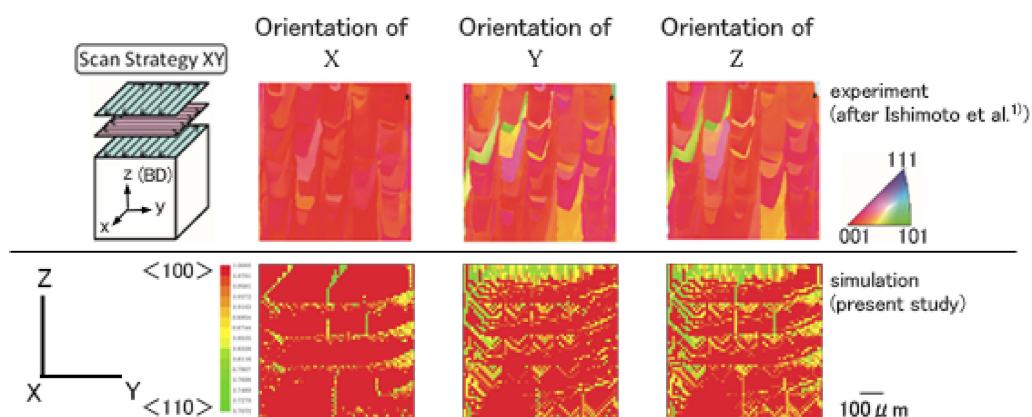


Fig. 10 Comparison of analysis results (lower side) with experimental results (upper side: after Ishimoto *et al.*¹⁾) of scan strategy XY.

- [275303](#).
- 15) T. Ishimoto, R. Ozasa, K. Nakano, M. Weinmann, C. Schnitter, M. Stenzel, A. Matsugaki, T. Nagase, T. Matsuzaka, M. Todai, H.-S. Kim and T. Nakano: *Scr. Mater.* **194** (2021) 113658.
- 16) B. Chalmers: *Principles of Solidification*, (John Wiley & Sons, Inc., New York, 1964) p. 263.
- 17) M.C. Flemings: *Solidification Processing*, (McGraw-Hill Book Company, New York, 1974) p. 135.
- 18) K. Kubo: *J. JFS* **83** (2011) 485–493.
- 19) K. Kubo: *J. JFS* **83** (2011) 533–538.
- 20) T. Ishimoto, S. Wu, Y. Ito, S.H. Sun, H. Amano and T. Nakano: *ISIJ Int.* **60** (2020) 1758–1764.